CrossMark
click for updates

Surface damage mitigation of Ti6Al4V alloy *via* thermal oxidation for oil and gas exploitation application: characterization of the microstructure and evaluation of the surface performance

Naiming Lin,*[abc] Qiang Liu,[a] Jiaojuan Zou,[a] Dali Li,[a] Shuo Yuan,[a] Zhihua Wang[b] and Bin Tang[a]

Because of its disadvantages of low surface hardness values, a high coefficient of friction and poor wear resistance, Ti6Al4V alloy is seldom used in tribological-related engineering components. To improve the surface performance of Ti6Al4V alloy used as petroleum tubes for oil and gas exploitation applications, a thermal oxidation (TO) process was applied to fabricate a TO layer on the Ti6Al4V substrate at 700 °C for 30 h. A microstructural characterization of the produced TO layer was systematically performed. Comparative estimations of the electrochemical corrosion, erosive-wear and corrosive-wear behaviors on the TO layers and Ti6Al4V alloys were conducted in CO_2-saturated simulated oilfield brine. The results showed that the obtained TO layer was mainly composed of rutile phase TiO_2 and minor anatase phase TiO_2. The continuous and compact TO layer reached a total thickness of about 20 μm. The TO layer contained an external oxide-layer and an internal O-diffusion layer. The concentration of O had a gradient descent along the thickness of the TO layer. The TO layer showed enhanced hardness and good bonding strength. Compared to the Ti6Al4V alloy substrates, the TO layers revealed superior surface performance in the electrochemical corrosion, erosive-wear and corrosive-wear tests. Excellent chemical stability, mechanical isolation action, high hardness and bonding strength contributed to the promising surface performance of the TO layer. TO treatment makes it possible to create a working surface on the Ti6Al4V alloy with enhanced surface hardness and wear resistance.

1. Introduction

Titanium and titanium alloys have been extensively applied in various fields of chemical industry, marine, aerospace and biomedical devices because of a specific combination of properties such as high strength to weight ratio, exceptional resistance to corrosion and excellent biocompatibility.[1–4] Recently, titanium alloys used as petroleum tubes have received great interest from material engineers after wide technical investigations and estimations.[5,6] However, the drawbacks of low surface hardness, high/unstable friction coefficient in sliding contacts against common bearing materials, severe adhesive wear and susceptibility to galling are harmful for the direct application of titanium alloys in oil/gas wells.[7–10] Numerous surface treatment technologies have been employed to improve the tribological performance of titanium and titanium

alloys.[11–15] Surface treatment can also make a favorable compromise between the cost and performance of engineering components by endowing the material surfaces with excellent corrosion resistance, high hardness/wear resistance, effective friction-reduction and promising mechanical performance without reducing the entire structure of the material.[16] A variety of surface treatment technologies, such as thermochemical surface treatment, micro arc oxidation (MAO)/plasma electrolytic oxidation (PEO), physical vapor deposition (PVD), chemical vapor deposition (CVD), ion implantation, thermal spraying, thermal oxidation (TO), laser surface treatment and electrospark deposition (ESD), and several duplex treatments have been conducted to improve the surface performance of titanium and its alloys.[17–30] Among the mentioned surface treatment technologies, thermal oxidation (TO) is an ideal surface technique that has been industrially used to strengthen the Ti-based materials.[31] Its popularity is mainly assign to its cost effectiveness, simplicity and rapidity. Furthermore, the TO treatment has no special requirements for substrate geometries.[32] TO process has been established in such a way that it can produce combined improvements in wear resistance and corrosion resistance, and successfully used for the surface treatment of Ti-

[a]*Research Institute of Surface Engineering, Taiyuan University of Technology, Taiyuan 030024, Shanxi, China. E-mail: lnmlz33@126.com; Tel: +86-351-6010540*

[b]*Shanxi Key Laboratory of Material Strength and Structure Impact, Taiyuan University of Technology, Taiyuan 030024, Shanxi, China*

[c]*Department of Chemical and Materials Engineering, University of Alberta, Edmonton, T6G 1H9, Canada*

based components for biological materials and some industrial fields.[31–41] Guleryuz, Wang and Borgioli et al. found that the tribological behaviors of the Ti6Al4V alloys were significantly improved after TO treatment.[42–44] Shankar and Jamesh et al. succeeded in enhancing the corrosion resistance of pure titanium and Ti6Al4V alloy in industrial acid environments via TO treatments.[45,46] Kumar and Çimenoğlu conducted TO treatments on Ti6Al4V and Ti6Al7Nb alloys for biological applications with great success.[47,48] Dearnley and Güleryüz et al. successfully obtained corrosive-wear resisting TO layers on commercial purity titanium and Ti6Al4V alloys by employing TO treatments.[49,50] Ebrahimi et al. confirmed that TO-treated samples exhibited better fatigue limits in comparison to untreated Ti-4Al-2V alloy.[51] Apart from common TO treatment, some novel TO-related treatments have also been proposed. Zhang et al. prepared a TO layer on Ti6Al4V alloy via a two-step treatment: the Ti6Al4V alloy was first TO treated in air and then diffusion treated in a vacuum. This process could harden a titanium surface deeply without inducing the scaling or oxide layer spallation associated with long time oxidation at high temperatures.[52] Sun et al. successfully conducted a duplex treatment on Ti6Al4V alloy via laser surface texturing (LST) and TO treatment. The excellent tribological performance of the duplex treated Ti6Al4V alloy was attributed to the strong bonding strength of the rutile film with a high hardness, promising ratio of hardness to elastic modulus and enhanced load-bearing capacity.[53] Vasylyev et al. developed an ultrasonic impact treatment induced oxidation on Ti6Al4V alloy, and a high performance surface was obtained on the treated Ti6Al4V alloy.[54]

In this study, Ti6Al4V alloys were firstly TO treated at 700 °C for 30 h. The microstructural characterizations of the TO layers were systematically investigated. Petroleum tubes suffer severe surface damage that mainly result from electrochemical corrosion, erosive-wear and corrosive-wear under complex and harsh work conditions in oil/gas wells.[55–59] In light of this, the electrochemical corrosion, erosive-wear and corrosive-wear behaviors of the TO layers and Ti6Al4V alloys were comparatively estimated. This work is expected to create a database and provide reference information for practical applications of TO-treated Ti6Al4V alloys in oil and gas exploitation applications.

2. Experimental

The specimens used for the experiments were prepared by an electro-spark wire-electrode cutting machine from a Ti6Al4V alloy rod, and the size was Φ 12 mm × 4 mm. The nominal chemical compositions (wt%) of the Ti6Al4V alloy was: Al 6.7; V 4.21; O 0.14; Fe 0.10; Si 0.07; N 0.015; H 0.003; C 0.003; Ti balance. Before TO treatments, the raw Ti6Al4V alloy samples were finely ground down to 800# using SiC abrasive papers followed by ultrasonic cleaning in acetone bath. The TO process was conducted in a muffle furnace at 700 °C for 30 h in air at atmospheric pressure (10^5 Pa). After the TO process, the treated samples were cooled at their own cooling rate in the furnace.

The phase constitutions of the received TO layer were identified by X-ray diffraction (XRD). Scanning electron microscopy

(SEM) with energy dispersive X-ray spectroscopy (EDS) and X-ray photoelectron spectroscopy (XPS) were employed to characterize the surface morphologies and surface elementary compositions of the Ti6Al4V alloy and TO layer. SEM and glow discharge optical emission spectrometer (GDOES) analyses were applied to investigate the cross-sectional morphology and elementary composition profile across the thickness of the TO layer.

A microhardness tester was used to measure the microhardness distribution across the cross section of the TO layer using a Vickers indenter under a load of 25 g applied for a dwell time of 20 s. Scratch and indentation tests were conducted to evaluate the bonding strength between the TO layer and the substrate using diamond indenters.[45,60]

The corrosion resistance of the TO layer was examined by electrochemical tests, including open-circuit potential (OCP) and potentiodynamic polarization.[45–47] The electrochemical experiments were performed on an electrochemical station using a traditional three-electrode cell. The reference electrode (RE) was a saturated calomel electrode (SCE), and the counter electrode (CE) was a platinum plate. The specimens of bare Ti6Al4V alloy and TO-treated Ti6Al4V alloy were used as the working electrodes (WE) with an exposed geometric area of 1 cm^2.

Erosive-wear tests were carried out on the Ti6Al4V alloy and TO layer in a liquid–solid two phase flow.[61–67] The erosive-wear apparatus mainly consisted of three parts, the revolving system, the sample-holding device and the barrel quartz container (Fig. 1). All the samples were fixed on the sample-holding device, and the fixed holding device was assembled to the revolving system. The fixed sample-holding device was totally immersed into the liquid–solid two phases flow-filled barrel quartz container. The revolving system of the erosion machine was driven by a motor with a speed of 200 rpm. The linear speed of slurry at the specimen surface was 3 m s^{-1}, and the testing duration was 120 h. Angular corundum particles in sizes ranging from 200–300 μm were used as the erodent to simulate the rock fragments generated during petroleum drilling exploiting. Actually, the liquid–solid two phase flow contains about 1 vol% rock chippings in real operating conditions, and corundum particles were artificially added up to 10 vol% to accelerate the slurry erosive-wear process in this work. An analytical balance with an accuracy of 0.01 mg was employed to weigh the original and erosive-worn samples. The surface morphologies of the erosive-worn samples were characterized using SEM and EDS.

The corrosive-wear resistance of the Ti6Al4V alloy and TO layer were evaluated by laboratory tests, which were performed on the MFT-R4000 friction-wear testing machine sliding against two counterparts in CO$_2$-saturated simulated oilfield brine (Fig. 2). High carbon chromium bearing steel balls (commonly referred as GCr15 in China with a hardness of about 700 HV, the nominal composition-wt% of GCr15 contains C: 0.95–1.05, Mn: 0.25–0.45, Si: 0.15–0.35, S: ≤0.025, P: ≤0.025, Cr: 1.40–1.65, Mo: ≤0.10, Ni: ≤0.30, Cu: ≤0.25, Fe balance) and silicon nitride (Si$_3$N$_4$ with a hardness more than 1500 HV) balls with a diameter of 5 mm were chosen as the counterparts. The two kinds of
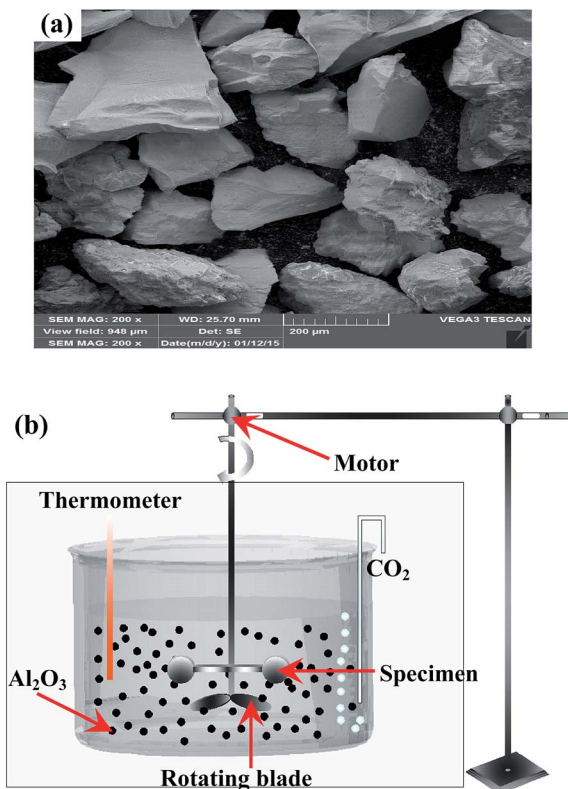
Fig. 1 SEM image of the angular brown corundum particles (a) and schematic diagram of the erosive-wear test device (b).
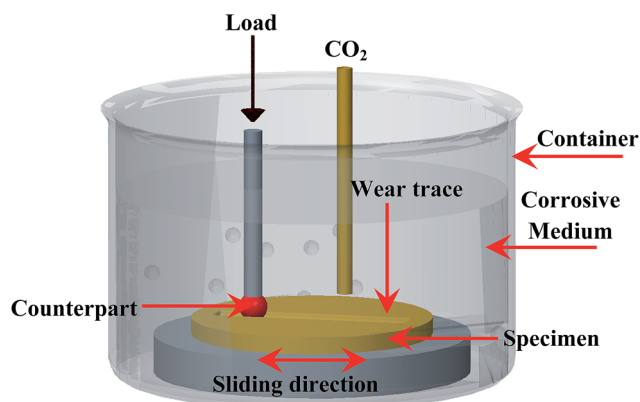

Fig. 2 Schematic diagram of the corrosive-wear test device.

ball counterparts were used as the upper specimens, and the Ti6Al4V alloy and TO-treated Ti6Al4V alloy operated as the lower specimens. For comparative purposes, all the corrosive-wear tests were conducted with the following identical parameters: a reciprocatory displacement of 5 mm, a normal load of 10 N, a reciprocatory frequency of 4 Hz, and a testing duration of 30 min. The wear resistance of the samples was defined by comparing the friction coefficients and mass losses. Specimens were thoroughly cleaned with acetone in an ultrasonic bath before and after the wearing tests. An analytical balance with an accuracy of 0.01 mg was employed to weigh the original and

corrosive-worn samples. The wear traces were also analyzed by using SEM and EDS. Meanwhile a white-light interfering profilometer was applied to observe the two-dimensional profiles and three-dimensional morphologies of the wear traces.[68–71]

In this work, a CO_2-saturated simulated oilfield brine (pH = 6.5) was used as the testing medium for the above three kinds of tests. It was made from analytical reagents and deionized water with a chemical composition (g L^{-1}) of 19 Cl^-, 1.14 SO_4^{2-}, 0.6 HCO_3^-, 0.12 CO_3^{2-}, 11.99 Na^+, 1.05 Mg^{2+}, and 0.39 Ca^{2+}.[72] CO_2 gas was passed through during the total testing period in the tests of electrochemical corrosion, erosive-wear and corrosive-wear. Additionally, the solution was renewed every 24 h to keep stable testing conditions for the duration of the erosive-wear tests.

3. Results and discussion

The microstructural characterizations of the produced TO layer are first presented in this section, and then, the electrochemical corrosion, erosive-wear and corrosive-wear behaviors of TO layers and Ti6Al4V alloys are subsequently described in Sections of 3.2, 3.3 and 3.4.

3.1 Microstructural characterizations

The XRD patterns of the TO layer and Ti6Al4V alloy are illustrated in Fig. 3. It was demonstrated that the peaks of the rutile phase TiO_2 (denoted as 'R' in Fig. 3) and anatase phase TiO_2 (denoted as 'A' in Fig. 3) were detected in the TO layer, and the rutile phase was the predominant phase in the obtained TO layer. Phase constitutions of the TO layer in this paper were in good agreement with Guleryuz and Kumar et al.'s work.[40,42,47] Seen from Fig. 3, there were obvious differences in the XRD patterns between the TO layer and Ti6Al4V alloy. Although the Ti6Al4V alloy is prone to form an oxide film, the self-formed oxide film was too thin to be reflected by XRD, and only the Ti peaks were characterized.[73,74]

Due to the interference of the incident light radiation and the thickness of the TO layer, the TO layer in this work presented a dark brown surface from macro observation, which was similar to Wang and Kumar et al.'s research.[43,47] Fig. 4 and 5 show the surface morphologies and compositions of the
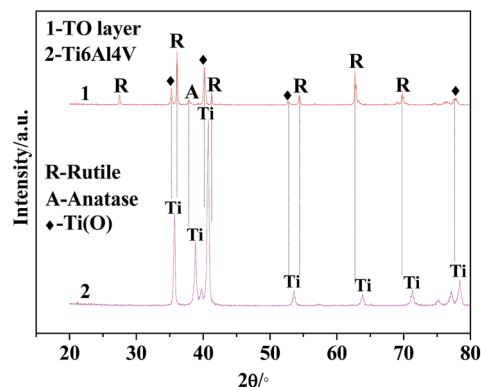

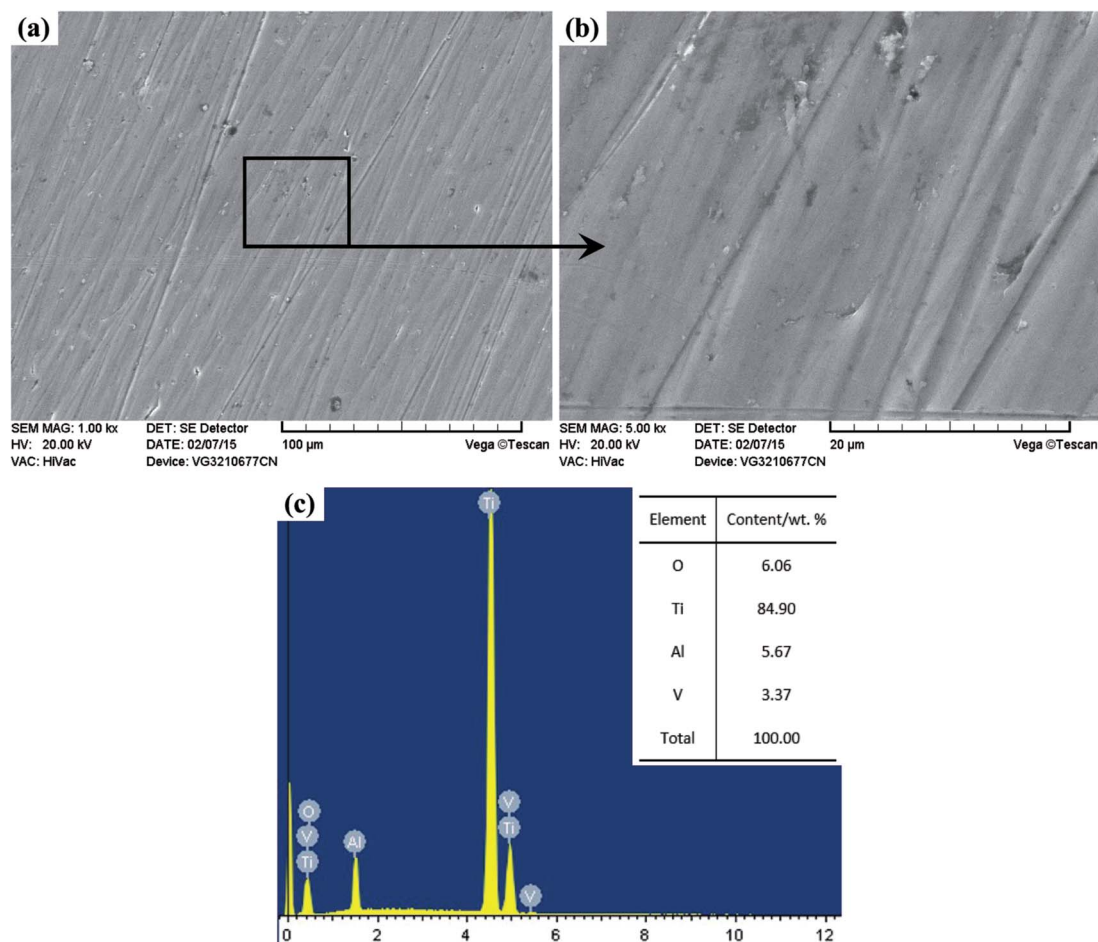Fig. 3 X-ray diffraction patterns of TO layer and Ti6Al4V alloy.

Fig. 4   Surface morphology and composition of the Ti6Al4V alloy.

Ti6Al4V alloy and TO layer. As the Ti6Al4V alloy could not withstand the damage from the abrasive particles during grinding, numerous parallel scratches can be found on the ground Ti6Al4V alloy surface in Fig. 4(a). Fig. 4(b) further reveals the damage degree after abrasive paper grinding on the surface of the Ti6Al4V alloy. It is seen in Fig. 4(c) that the elements of Ti, Al, V and minor O were detected by EDS analysis. It can be found that the contents of Ti, Al and V were close to the standard contents in Ti6Al4V alloy. Although Ti6Al4V alloy is prone to passivation, the formed oxide film usually reaches a nano-scale on the surface; hence, a low content of O was collected.[52] As presented in Fig. 5(a), the original scratches seem unclear, and only a few deep scratches are observable on the surface of the TO layer. However, these scratches on the TO layer surface are still more shallow when compared to the scratches on the Ti6Al4V alloy surface. Fig. 5(b) indicates the higher relative intensities of Ti, Al and O compared to Fig. 4(c) according to the EDS analysis. When comparing Fig. 4(c) with Fig. 5(b), it is noticeable that the content of O on the Ti6Al4V alloy surface formed *via* self-passivation was far lower than that of the TO layer. It was confirmed that more aluminium and titanium oxides were formed on the external surface of the TO layer after TO treatment. As shown in Fig. 5(c) and(d), the TO layer was dense and continuous. Many oxide grains and islands can be

found, and there was no cracking or spallation on the surface, which clearly demonstrated that the oxides grew outwardly and covered all of the Ti6Al4V alloy surface after TO treatment. Fig. 5(e) and (f) also suggest the local agglomeration of fine oxide grains on the surface of the TO layer. Fig. 5(e) and (f) show that some oxide particles on the outside surface of the TO layer are nano-scale. Fig. 5(g), which was obtained using atomic force microscope (AFM), further revealed that the larger oxide particles in the sizes of tens to hundreds of nanometers were composed of smaller oxides. Generally, a complete TO process of metals contains five steps: absorption of O → dissolution of O → formation of thin oxide film → growth of oxide layer → formation of thick oxide layer.[36,43,75] Wang and Kumar *et al.* reported that the growth of the oxides and formation of the TO layer were dependent on the temperature and duration of the TO processes.[36,43,47] According to their research, the adopted process parameters and cooling mode in our work are favorable for a promising TO-treated Ti6Al4V alloy for oil and gas exploitation applications.

Fig. 6(a) presents the XPS survey spectra of the TO layer and Ti6Al4V alloy. The survey spectra indicate the presence of Ti, Al, V, O and C. These elements are consistent with those obtained in the EDS analysis except for C. The O 1s peak at 529.3 eV can be assigned to the lattice oxygen atom of TiO_2 on
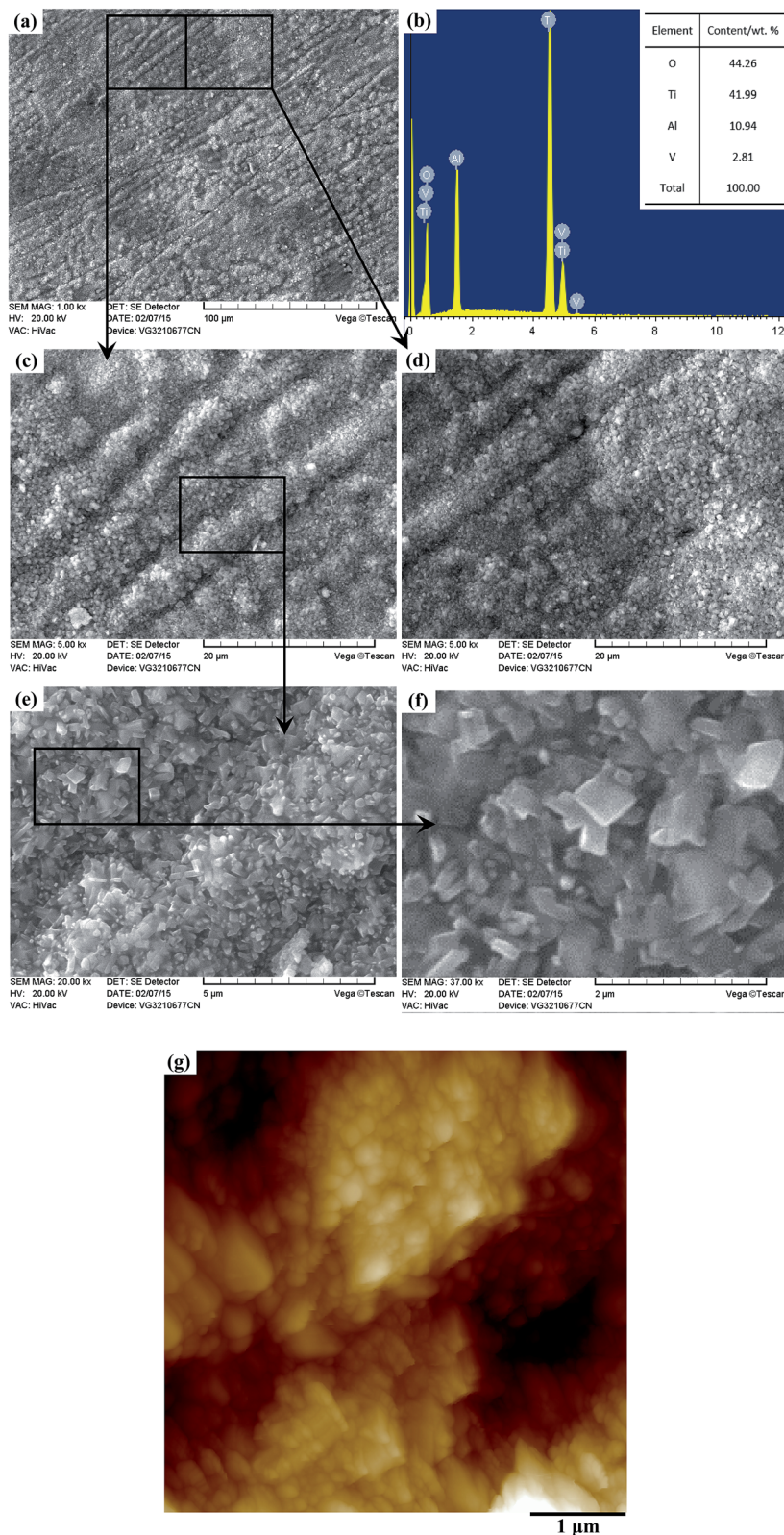
Fig. 5 Surface morphology and composition of the TO layer.

the TO layer, and the peak at 531.1 eV is closely related to the hydroxyl groups (–OH) resulting mainly from the chemisorbed water on the Ti6Al4V alloy. In addition, there is a peak at

517.2 eV for the TO layer, which might be attributed to the formation of vanadium oxide V_2O_3. Meanwhile the variations in the binding energy values of O 1s and Ti 2p between the TO
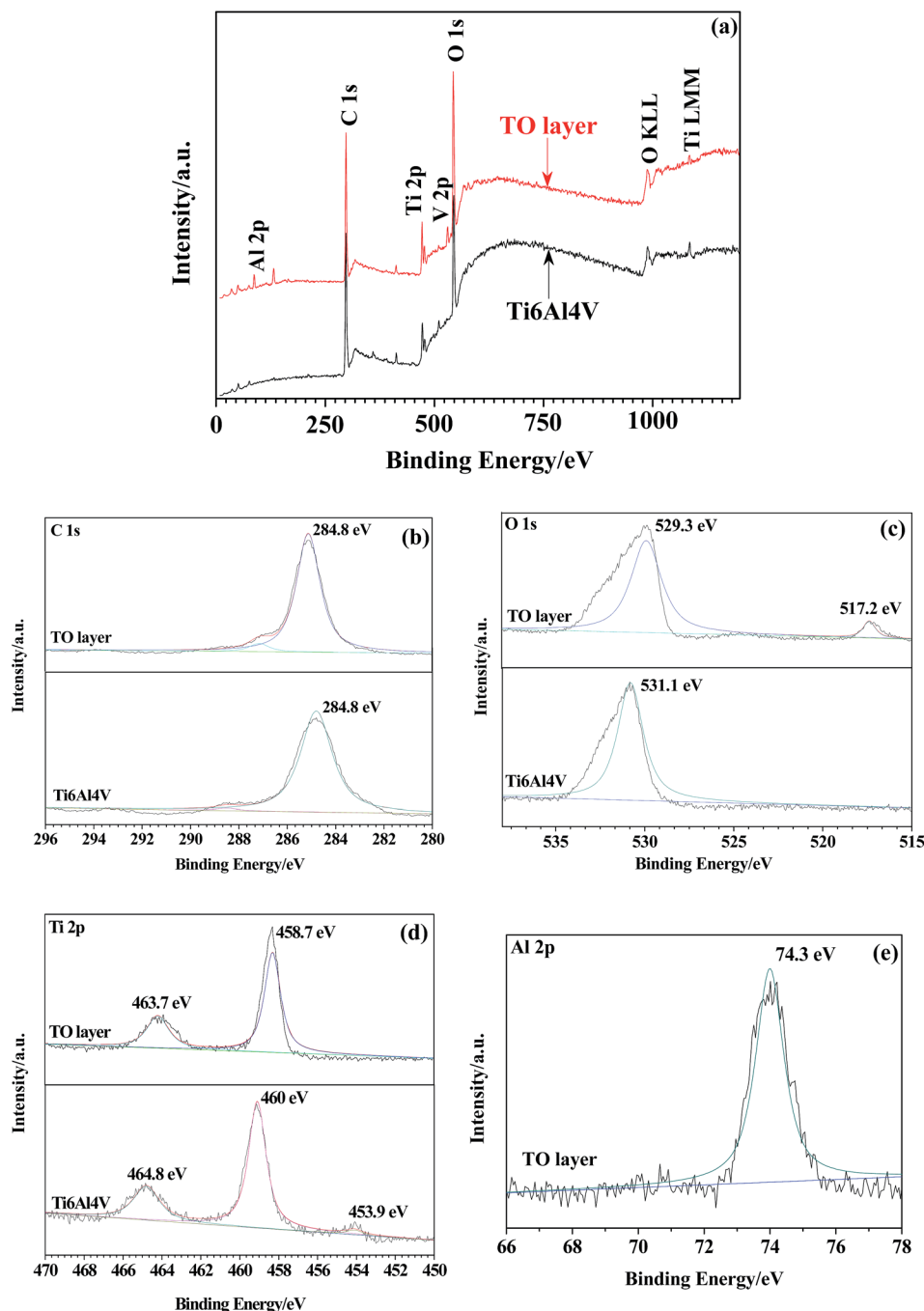
Fig. 6 XSP survey spectra of the TO layer and Ti6Al4V alloy (a) and XPS spectral detailed spectra collected from the TO layer and Ti6Al4V alloy: C 1s (b), O 1s (c), Ti 2p (d), Al 2p (e).

layer and Ti6Al4V alloy, as shown in Fig. 6(c) and (d), also confirmed the abundant formation of the R-dominated TiO_2 layer after TO treatment at 700 °C for 30 h.[75–78] Fig. 6(e) shows a few kinds of alumina (Al_2O_3) phases were also detected by XPS, which means there was also an oxidation reaction between Al and O in the TO process.[79]

For microstructural observations, the metallographic cross section of the TO layer was prepared using a standard conventional procedure and etched in a Kroll solution. Fig. 7 shows the cross-sectional morphology of the obtained TO layer, and it can

be seen that the TO layer was uniform and continuous. The TO layer revealed better corrosion resistance than the Ti6Al4V alloy to the Kroll solution, which is indicated by a bright feature. There were no pores or cracks in the TO layer, and the Ti6Al4V alloy substrate was well covered by the TO layer. The TO layer can play a positive role in preventing the Ti6Al4V alloy from degradation during operation. According to the scale in Fig. 7, the bright zone reached a thickness of less than 10 μm; however, this does not mean that the thickness value of the received total TO layer was no more than 10 μm. It is well accepted that
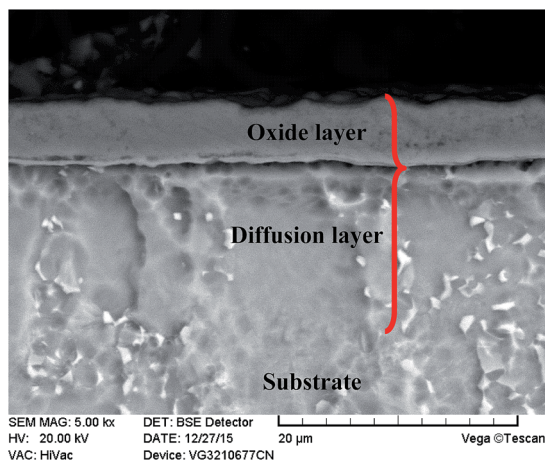
Fig. 7 Cross-sectional morphology of the TO layer.

a complete TO layer is composed of an external oxide layer and a diffusion layer beneath.[36,43,47]

The GDOES was applied to investigate the composition profile and the thickness of the TO layer. The GDOES composition profile–distance from the surface of the TO layer is suggested in Fig. 8, and O, Ti, Al and V were detected through the thickness of the TO layer. Fig. 8 shows that the concentration of O gradually decreases, while the concentration of Ti tends to increase from the surface to the interior. The maximum content of O in the TO layer is more than 90 wt% according to the GDOES result. The total thickness of the TO layer was approximately 20 μm, as derived from the GDOES analysis of the cross-section. As shown in Fig. 8, Al shows a relatively high concentration in the very first 2 μm and a relatively low concentration in the distance zone of 5–15 μm compared to its original content in the Ti6Al4V alloy. That was attributed to the external migration of Al, and external migration of Al in Ti6Al4V alloy was found in our previous processing research work on TO treatment.[72] The concentration of V was almost the same in the GDOES analysis, and the content of V in the Ti6Al4V alloy and its chemical properties resulted in the composition distribution of V in the TO layer.[80]
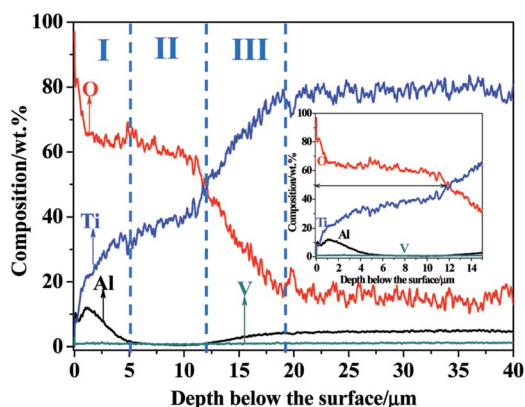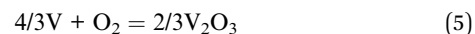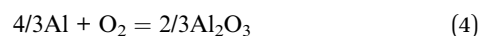
Under permanent temperature and pressure conditions, the standard Gibbs energy change (ΔG_{T}^0) can be obtained from the following equation:[80]

$$\Delta G_{\mathrm{T}}^0 = \Delta H_{298}^0 - T\Delta S_{298}^0 + \int_{298}^T \Delta C_{\mathrm{p}}\mathrm{d}T - T\int_{298}^T \frac{\Delta C_{\mathrm{p}}}{T}\mathrm{d}T \quad (1)$$

where ΔH_{298}^0 is the standard free energy of formation at 298 K (kJ mol^{-1}), T the is temperature in Kelvin, ΔS_{298}^0 is the standard absolute entropy at 298 K, and ΔC_{p} is the heat capacity. Eqn (1) can be further simplified as follows:

$$\Delta G_{\mathrm{T}}^0 = \Delta H_{298}^0 - T\Delta S_{298}^0 \quad (2)$$

The oxidation reactions of Ti, Al and V with O are shown in eqn (3)–(5):[80]

$$\mathrm{Ti} + \mathrm{O}_2 = \mathrm{TiO}_2 \quad (3)$$

$$4/3\mathrm{Al} + \mathrm{O}_2 = 2/3\mathrm{Al}_2\mathrm{O}_3 \quad (4)$$

$$4/3\mathrm{V} + \mathrm{O}_2 = 2/3\mathrm{V}_2\mathrm{O}_3 \quad (5)$$

For all the reactions, the values of ΔG_{T}^0 belonging to TiO$_2$, Al$_2$O$_3$ and V$_2$O$_3$ can be calculated according to eqn (2). The values of ΔG_{T}^0 can be applied to determine the feasibility of oxidation reactions and the relative stability of oxides. The obtained values are presented as follows: TiO$_2$ ($\Delta G_{\mathrm{T}}^0 = -960.76$), Al$_2O_3$ ($\Delta G_{\mathrm{T}}^0 = -1146.28$) and V$_2O_3$ ($\Delta G_{\mathrm{T}}^0 = -872.96$). According to the values of ΔG_{T}^0, Al is the most prone to oxidation followed by Ti and V. Meanwhile, the position of Al in the periodic table is in front of Ti and V. Therefore, external migration of Al is possible from a thermodynamic point of view.[81,82] Al peaks were detected in the EDS and XPS analyses; however, the Al$_2$O$_3$-rich zone distributed in the near surface of the TO layer was too thin to be characterized by XRD. Ti is next to V in the periodic table, and the content of V in the Ti6Al4V alloy is the lowest. In addition, the ΔG_{T}^0 of V$_2$O$_3$ is the highest, which means it is the hardest to form an oxide among the three elements in the Ti6Al4V alloy. Seen from Fig. 8, based on the GDOES composition profile, the whole TO layer can be divided into three parts as the dotted lines indicate. As combined with the analysis results of EDS (Fig. 5) and XPS (Fig. 6), zone-I, which consisted of Al$_2$O$_3$ and TiO$_2$, was an Al-rich zone, and zone-II, which was poor in Al, was mainly built up by TiO$_2$ with minor V$_2$O$_3$. For the whole TO layer, zone-I and zone-II corresponded to the oxide layer, and zone-III was corresponded to the O-diffusion layer.[36,43,47]

In accordance with the microhardness corresponding to the measuring points along the depth direction of the TO layer, the microhardness distributing curve of the TO layer was plotted, as shown in Fig. 9. It is noted that the maximum hardness value of the TO layer is more than two folds harder than the Ti6Al4V alloy. The hardness distribution of the TO layer decreased gradually from the external surface to the inside of the TO layer. Considerable enhancement in microhardness is connected with structural modification on the near surface of the Ti6Al4V alloy, which resulted from the formation of oxides (Al$_2$O$_3$ and TiO$_2$) in the TO layer.[40,42,44,49]

Fig. 8 GDOES composition profile–distance from the surface of the TO layer.
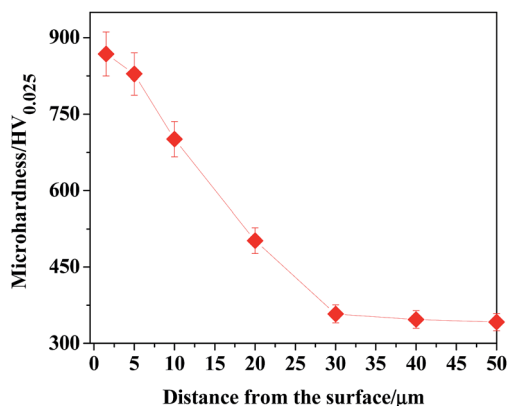
Fig. 9 Microhardness distribution–distance from the surface of the TO layer.

The scratch test is a widely used method for testing the adhesion of the coating/film.[45,83] Fig. 10 shows the collected acoustic emission intensity–normal load curve during the scratch test. As given in Fig. 10, the acoustic emission signals clearly notify that the failures occurred at lower loads (0.5 to 4 N) in zone-A. As 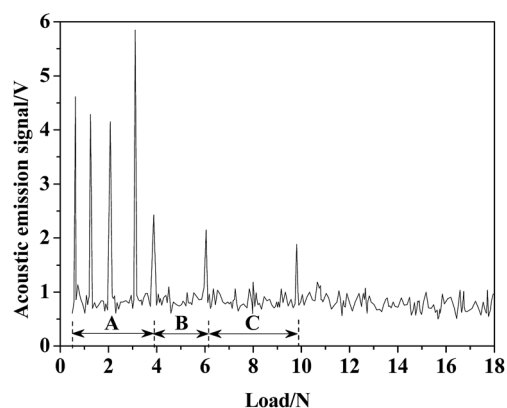the external migration of Al, zone-I in Fig. 9, which was composed of Al_2O_3 and TiO_2, corresponded to zone-A in Fig. 10. There was a significant difference in the crystalline structure between Al_2O_3 and TiO_2, and this hybrid oxide layer indicated insufficient resistance to the scratch. Zone-II in Fig. 9 was poor in Al, and it mainly contained pure R-phase TiO_2 and revealed a better scratch resistance, reflecting the collected acoustic emission signal under a higher load in Fig. 10 (zone-B). As shown in Fig. 10, the TO layer was completely destroyed under a load of 10 N, which means the bonding strength of the obtained TO layer was about 10 N. Zone-C in Fig. 10 corresponds to zone-III in Fig. 9.

Fig. 11 presents the scratch morphology of the TO layer. Seen from Fig. 11, the scratch morphology of the TO layer was consistent with the acoustic emission signals in Fig. 10. Meanwhile, the cracks caused by tensile stresses can be found in the scratch trace perpendicular to the scratch direction, which means brittle fracture occurred on the oxide layer. EDS analysis results of selected regions in Fig. 11 are given in Table 1, and EDS analysis provided a promising complementary description of the scratch behavior and further confirmed the complete failure of the TO layer.[45,84]

Fig. 12 shows the Rockwell indentation morphologies of the TO layer under loads of 588 N (a) and 1471 N (b), and a higher load produced a bigger crater. It is evident that radial cracks can be found around the indentation craters after the Rockwell indentation tests in Fig. 12. It is also clearly observable that the TO layer exhibits local layer delamination after indentation, and the peeled area was larger as the applied load increased. According to the VDI3198 standard ("HF classes"), the bonding strength values of the TO layer under loads of 588 N and 1471 N were HF 3 (588 N) and HF 4 (1471 N), respectively. The EDS analysis results of the selected regions on the surface of the TO

Fig. 10 Relationship between acoustic emission intensity and normal load.

Table 1 EDS analysis of the scratched TO layer surface (wt%)

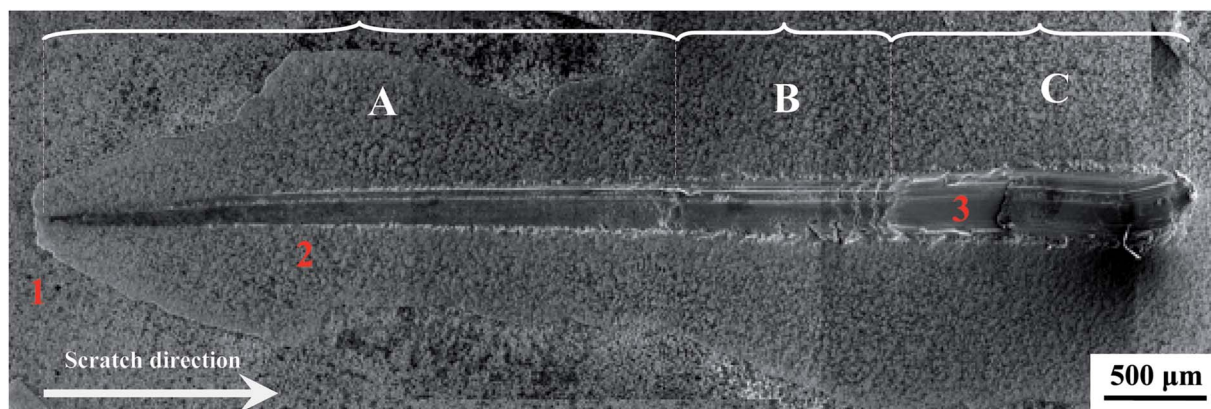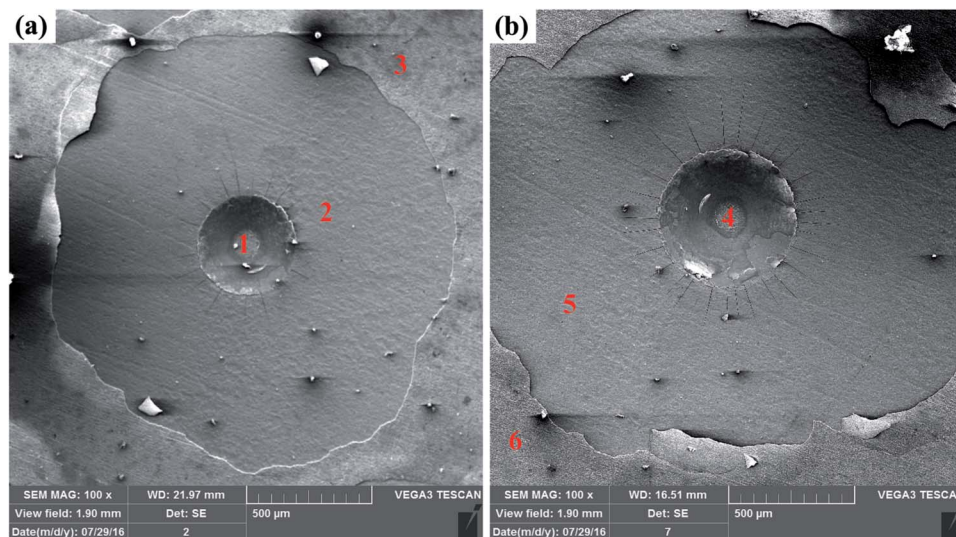| Element	O	Ti	Al	V
Zone-1	44.24	42.63	10.25	2.88
Zone-2	33.55	60.61	3.67	2.17
Zone-3	—	91.17	5.67	3.16

Fig. 11 Scratch morphology of the TO layer.

Fig. 12 Indentation morphologies of the TO layer: 588 N (a) and 1471 N (b).

layer after the Rockwell indentation tests are suggested in Table 2. Combing the indentation morphologies in Fig. 12 and the EDS analysis results in Table 2, it is certain that the Al_2O_3 and TiO_2 hybrid oxide layer was totally destroyed after the Rockwell indentations, which was ascribed to the significant difference in the crystalline structure between Al_2O_3 and TiO_2. However, the TO_2 layer with a certain hardness and the O-diffusion layer with a gradient compositional distribution can have a protective effect against indentation. The TO layer was

not completely destroyed, and the Ti6Al4V was not exposed after the Rockwell indentations in accordance with the EDS analysis in the centre of the indentation craters.[60,83,84]

3.2 Electrochemical behavior

The OCPs of the TO layer and Ti6Al4V alloy were recorded as a function of the immersion time over a period of 3600 s in CO_2-saturated simulated oilfield brine, as shown in Fig. 13. Overall it is seen that both the OCPs showed a rising trend with increasing immersion time. After the tested samples of the TO layer and Ti6Al4V alloy were immersed in the selected solution for 3600 s, the OCP of the TO layer began to shift towards more positive values until it stabilized and reached an OCP of 0.483 V; the OCP of Ti6Al4V alloy started at a less negative potential and kept on increasing up to −0.0824 V. A higher OCP for the obtained TO layer in the Cl-containing medium is consistent with Jamesh *et al.*'s study.[85] The OCP can be used to evaluate the chemical stability and corrosion process of the experimental samples, and the change in the OCP is also assumed to be

Table 2 EDS analysis of the indented TO layer surface (wt%)

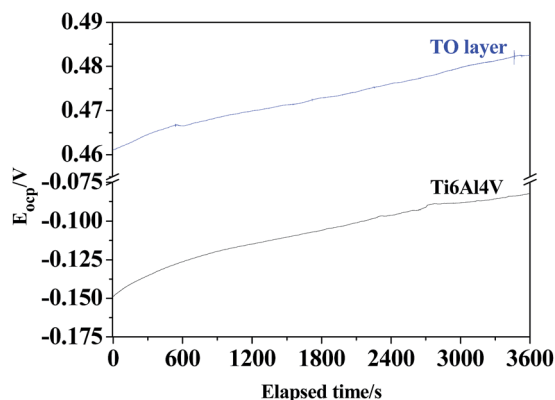| Element		O	Ti	Al	V
Fig. 12(a)	Zone-1	51.21	36.39	10.17	2.23
	Zone-2	28.67	64.51	4.78	2.04
	Zone-3	49.40	37.48	10.81	2.31
Fig. 12(b)	Zone-4	49.73	39.07	8.98	2.22
	Zone-5	29.44	64.62	3.82	2.12
	Zone-6	48.03	40.81	8.89	2.27

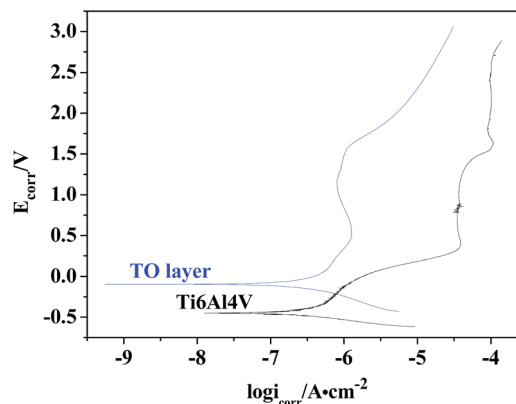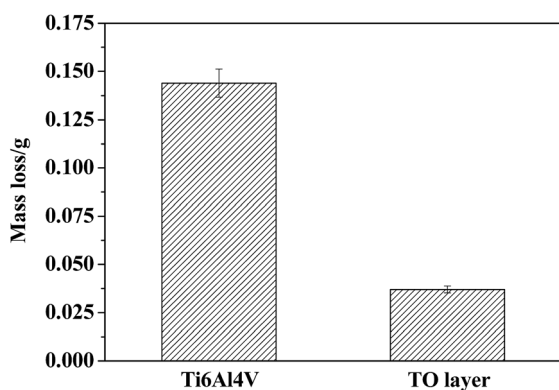Fig. 13 OCP−time curves of the TO layer and Ti6Al4V alloy.

Fig. 14 Polarization curves of the TO layer and Ti6Al4V alloy.

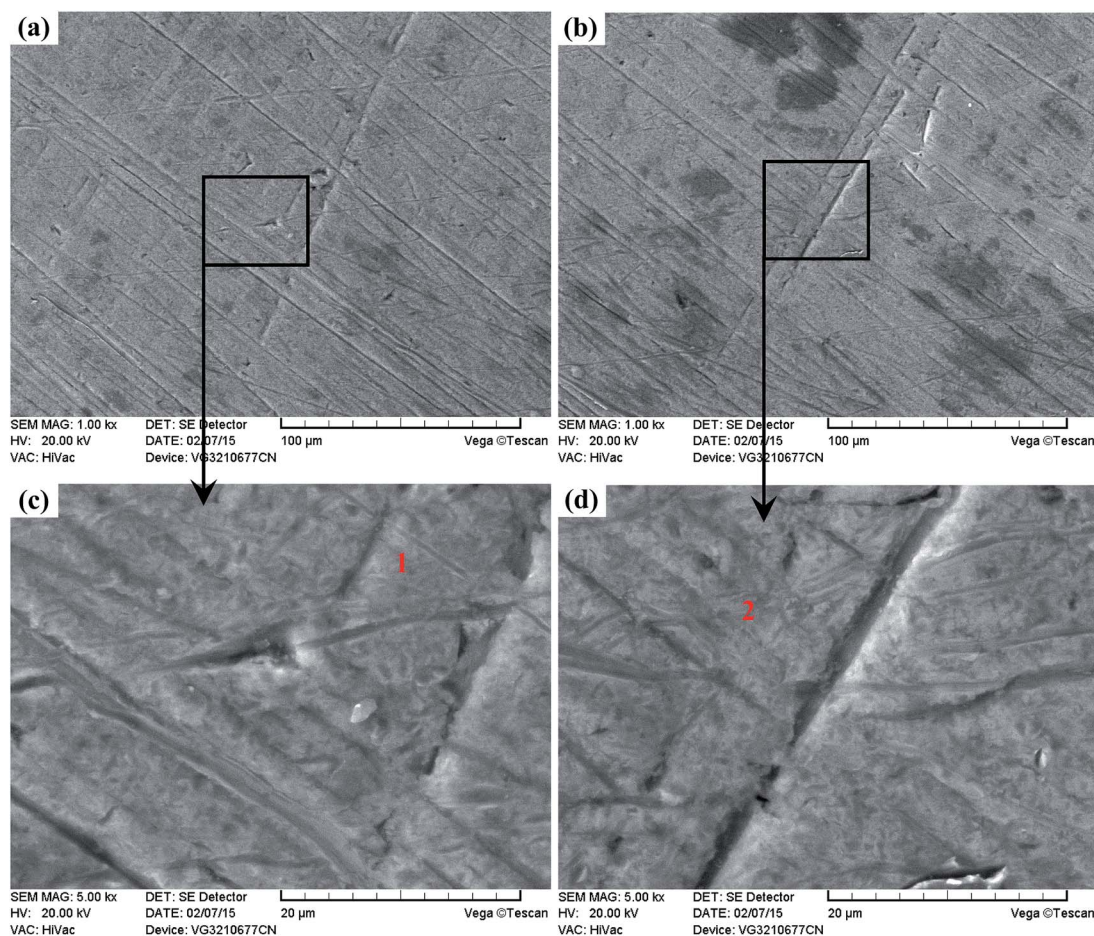**Table 3** Results of the open circuit potential and polarization tests

Item	Ti6Al4V alloy	TO layer
E_{ocp}/V	−0.0824	0.483
E_{corr}/V	−0.450	−0.0987
I_{corr}/A cm^{-2}	2.361×10^{-7}	2.595×10^{-7}
I_{pass}/A cm^{-2}	6.018×10^{-5}	8.980×10^{-7}

related to the growth and stability of the corrosion scale on the testing material surface.[86] The variation in trends of the OCPs of the TO layer and Ti6Al4V alloy in Fig. 13 indicates that both of them underwent a decrease in the corrosion tendency from a thermodynamic view. Additionally, it was noted that the TO layer had a nobler potential than the Ti6Al4V alloy substrate, which means the TO layer was more stable than the Ti6Al4V alloy.[87–89]

The potentiodynamic polarization curves for the TO layer and Ti6A14V alloy substrate in CO_2-saturated simulated oilfield brine, presented in a semi-logarithmic scale, are shown in Fig. 14. As shown in Fig. 14, the plot of the TO layer displays a marked shift towards the nobler direction in comparison to the Ti6A14V alloy. Meanwhile, seen from Fig. 14, obvious passivation zones can be found in both of the two polarization curves. The corrosion potentials (E_{corr}) and corrosion current densities (I_{corr}) were obtained by extrapolating the rectilinear Tafel segments of the anode and cathode polarization curves, and passivation current densities (I_{pass}) were read from the passivation zones in the polarization curves.[89–91] All of the electrochemical testing results are listed in Table 3. As suggested in Table 3, the TO layer reveals a more positive E_{corr} than that of the Ti6A14V alloy, and the I_{corr} belonging to the TO layer was even slightly higher than that of the Ti6A14V alloy.

Fig. 15 Column charts of mass losses of the TO layer and Ti6Al4V alloy after erosive-wear tests.

Fig. 16 Surface morphologies of the erosive-worn Ti6Al4V alloy.

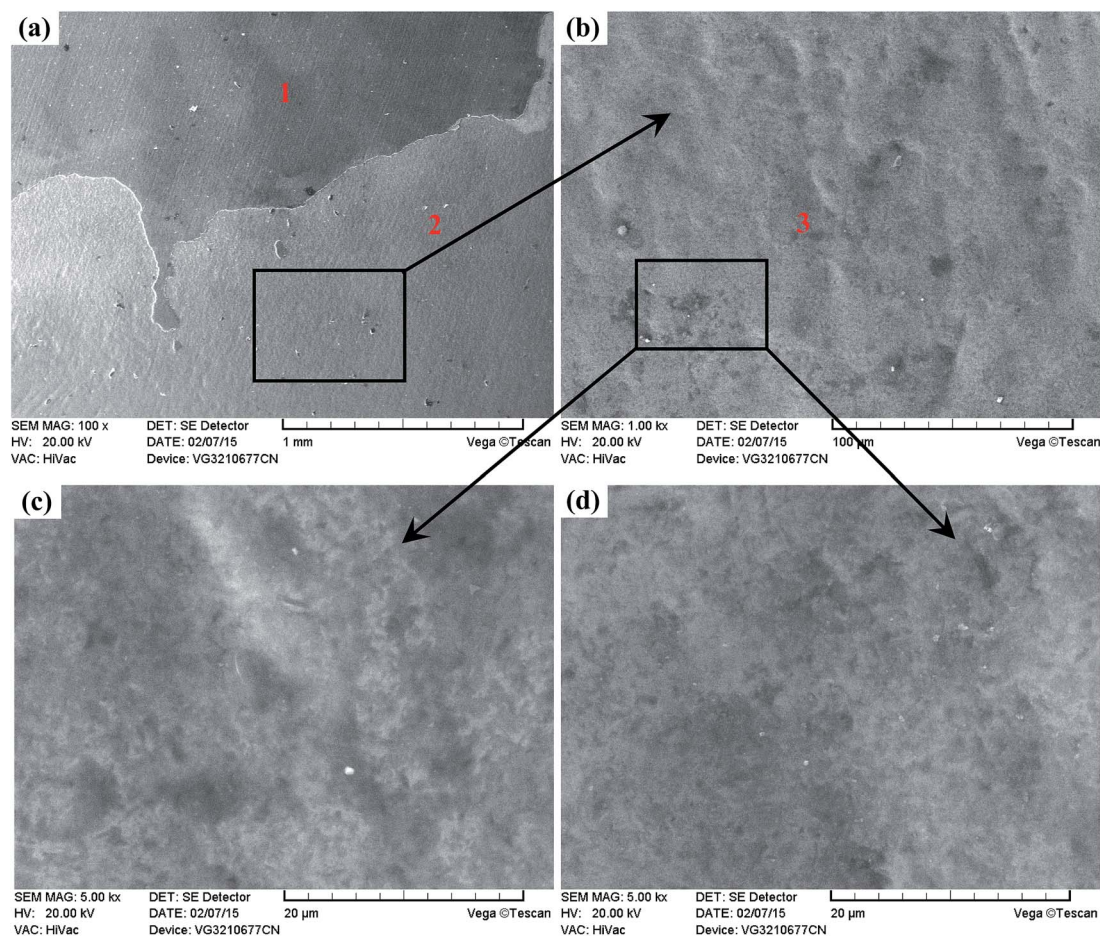This journal is © The Royal Society of Chemistry 2017

Fig. 17 Surface morphologies of the erosive-worn TO layer.

However, the two I_{corr} were on the same order of magnitude. In the previous research, most of the results showed that a TO layer had a rougher surface than the ground Ti6A14V alloy, which meant that the TO layer had a high specific surface area.[42–44] Therefore, the TO layer had a larger real area than the Ti6A14V alloy on the surface that contacted the corrosion medium, which resulted in a slightly higher I_{corr}. Fig. 14 also indicates that the TO layer had a far lower I_{pass} than that of the Ti6A14V alloy, which means that the TO layer had a lower electrochemical active behavior even though it showed a slightly higher I_{corr}.[47] The received TO layer, which had a certain thickness and consisted of R-phase TiO_2, acted as a protective layer and protected the Ti6A14V alloy substrate from the Cl^- attacking.[87–91]

3.3 Erosive-wear behaviours

Fig. 15 displays the column charts of the mass losses of the Ti6A14V alloy and TO layer after erosive-wear tests. It is noticeable that the mass loss of Ti6A14V alloy is nearly three times higher than that of the TO layer in Fig. 15. A higher surface hardness favoured the erosive-wear performance of the TO layer.[39,41,43]

Fig. 16 and 17 present the surface morphologies of the Ti6A14V alloy and TO layer at different magnifications after erosive-wear tests. Meanwhile, the elemental concentrations in typical zones on the tested samples were characterized by EDS to provide supplementary information to elucidate the deterioration mechanisms, and the results are given in Tables 4 and 5. Fig. 16 reveals that the Ti6A14V alloy suffered certain damage after erosive-wear compared to the ground Ti6A14V alloy in Fig. 4. Seen from Fig. 16(a) and (b), besides the grinding scratches on the surface of the Ti6A14V alloy, discrete lips and craters that are produced by erosive-wear from angular brown corundum particles are noticeable. Fig. 16(c) and (d) present the

Table 4 EDS analysis of the erosive-worn Ti6Al4V alloy surface (wt%)

Element	O	Ti	Al	V
Zone-1	6.31	84.86	5.67	3.16
Zone-2	4.24	87.69	5.96	2.11

Table 5 EDS analysis of the erosive-worn TO layer surface (wt%)

Element	O	Ti	Al	V
Zone-1	44.24	42.63	10.25	2.88
Zone-2	40.67	48.12	8.63	2.58
Zone-3	39.24	49.69	8.82	2.25

in situ high magnification images of the rectangular area zone in Fig. 16(a) and (b), where the lips and craters are further highlighted. Clearly, Ti6Al4V received micro-cutting from the brown corundum particles. Table 4 shows the EDS analysis of the selected zones on the erosive-worn Ti6Al4V alloy surface. As the Ti6Al4V alloy is prone to passivating, some amount of O was detected on its erosive-worn surface. As shown in Fig. 17(a), local layer delamination can be found on the surface of the TO layer after erosive-wear. Seen from Fig. 17(b)–(d), the erosive-worn surface of the TO layer is smooth, and there are no lips or craters. As the Al_2O_3 and TiO_2 hybrid layer was locally removed, the exposed TO layer suffered polishing-like grinding from the brown corundum particles. Table 5 shows the EDS analysis of selected regions on the erosive-worn TO layer surface. According to the EDS analysis results, the region-1 and region-2 in Fig. 17(a) corresponded to zone-I and zone-II in Fig. 8, respectively. Based on the EDS analysis of region-2 and region-3 in Table 5, it is certain that the TO layer was not completely destroyed. Generally, the metal oxide has a higher molecular weight than elemental metal, therefore the TiO_2 is heavier than Ti at the same volume.[80] Fig. 15 has indicated the mass losses of the TO layer were far lower than that of the Ti6Al4V alloy, which means there was less volume loss of the TO layer in comparison to the Ti6Al4V alloy. By comparing the results obtained from Fig. 15–17, one can see that the TO layer

had better erosive-wear resistance than the Ti6Al4V alloy under the testing conditions. The excellent erosive-wear performance of the TO layer benefited from its good chemical stability and high hardness.[61–68,88,92,93]

3.4 Corrosive-wear behaviours

Fig. 18 shows the variations in the coefficient of friction (COF) during sliding processes against GCr15 and Si_3N_4 in CO_2-saturated simulated oilfield brine for the Ti6Al4V alloy and TO layer. In general, the received COF values of the Ti6Al4V alloy and TO layer after corrosive-wear were lower than those collected after the sliding tests in air.[94,95] The corrosion medium caused a certain friction-reduction effect on the tested samples.[49,50] Seen from Fig. 18(a), the TO layer presented a higher COF than the Ti6Al4V alloy through the sliding time as they were tested against GCr15. However, the Ti6Al4V alloy indicated a higher COF than that of the TO layer for the whole sliding time when they were paired with Si_3N_4, as shown in Fig. 18(b). The differences in the COF values of the Ti6Al4V alloy and TO layer between the two counterparts were attributed to the different wear mechanisms of the Ti6Al4V alloy and TO layer in the tests.[3] The variations can also be found in the mass loss after the corrosive-wear tests in Fig. 19. As suggested in Fig. 19(a), the TO layer indicated a negative mass loss and the Ti6Al4V alloy showed a mass loss of about 0.4 mg when they were paired with
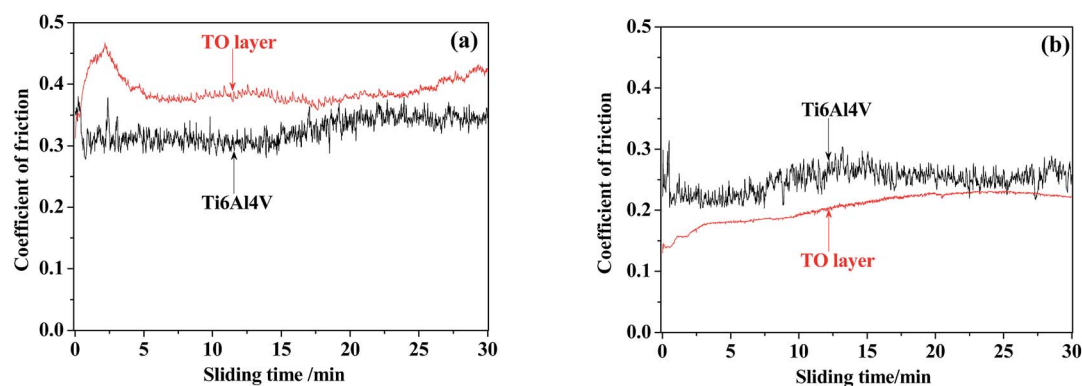

Fig. 18 Coefficients of friction for the TO layer and Ti6Al4V alloy sliding against GCr15 (a) and Si_3N_4 (b).
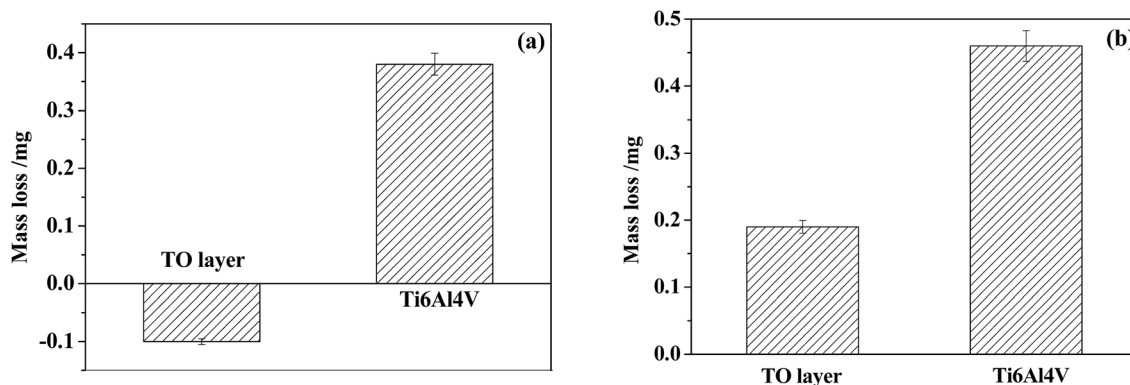

Fig. 19 Mass losses of the TO layer and Ti6Al4V alloy sliding against GCr15 (a) and Si_3N_4 (b).
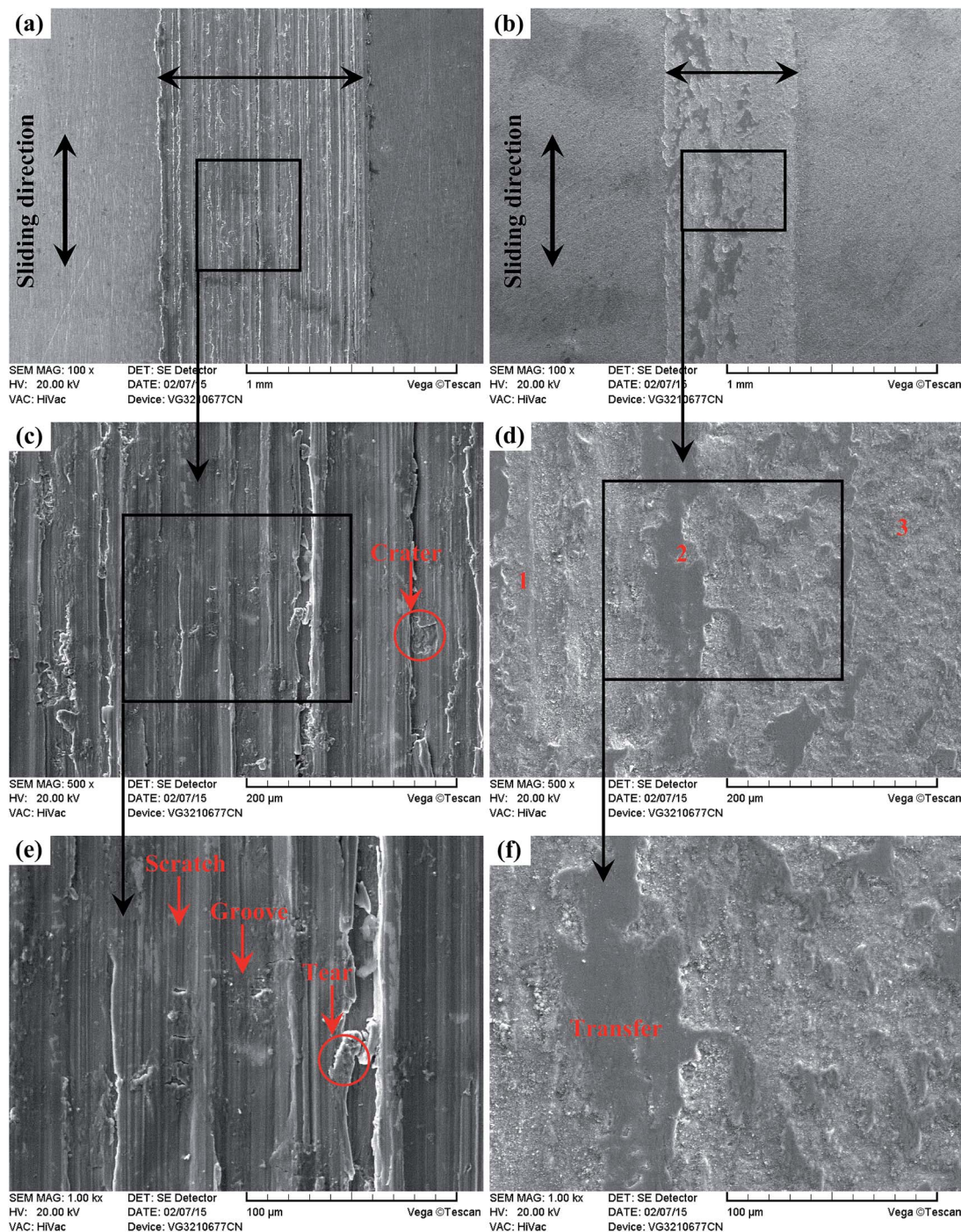
Fig. 20   Wear traces of the Ti6Al4V alloy (a) (c) (e) and TO layer (b) (d) (f) sliding against GCr15.

GCr15. Fig. 19(b) shows that the Ti6Al4V alloy indicated a significantly higher mass loss than that of the TO layer as they were tested with Si_3N_4. Meanwhile, different wear modes of the

Ti6Al4V alloy and TO layer are also responsible for their distinctions in mass loss.[57] Since the TiO_2 has a higher molecular weight than Ti, the TiO_2 is certainly heavier than Ti at the

Table 6 EDS analysis of corrosive-worn TO layer surface sliding against GCr15 (wt%)

Element	Fe	O	Ti	Al	V
Zone-1	11.16	41.14	37.13	8.25	2.32
Zone-2	68.18	19.34	9.22	3.13	0.13
Zone-3	5.46	39.24	44.23	8.82	2.25

Table 7 EDS analysis of corrosive-worn TO layer surface against Si_3N_4 (wt%)

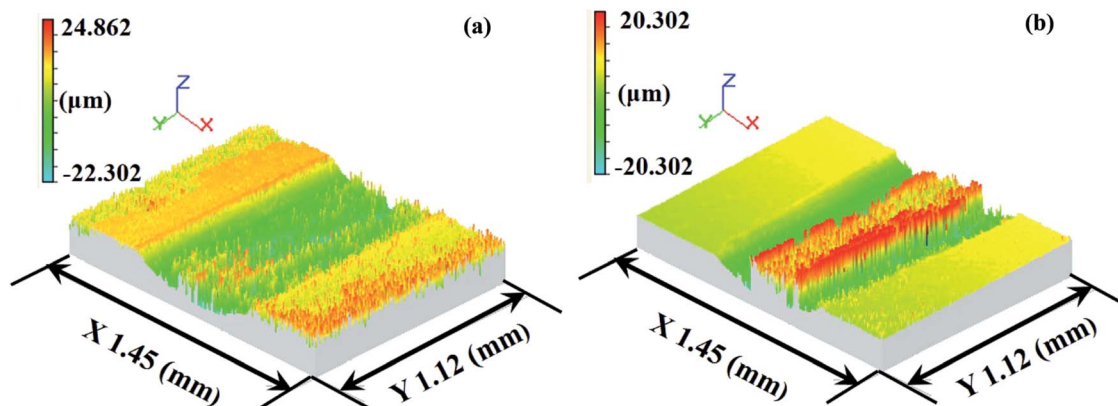| Element	O	Ti	Al	V
Zone-1	42.98	43.49	10.71	2.82
Zone-2	37.68	50.12	9.64	2.56
Zone-3	21.32	72.22	3.92	2.54

Fig. 21 White-light interferometer wear traces of the Ti6Al4V alloy (a) and TO layer (b) sliding against GCr15.
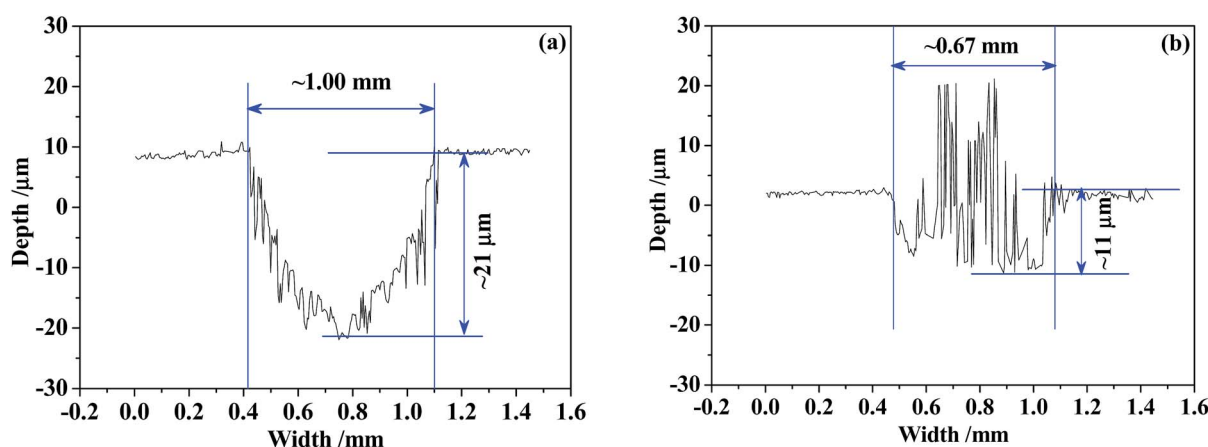

Fig. 22 Wear trace profiles of the Ti6Al4V alloy (a) and TO layer (b) sliding against GCr15.

same volume.[80] Lower mass losses of the TO layer corresponded to the wear volumes, which can be reflected by the wear trace profiles.

Aiming to realize better visualizations of the corrosive-worn surfaces and interpretation of the wear mechanisms, the corrosive-worn surface morphologies of the Ti6Al4V alloy and TO layer at different scales were obtained by SEM (see Fig. 20 and 23). Meanwhile, the elemental concentrations in typical zones on the corrosive-worn TO layers were characterized using EDS to provide supplementary information to elucidate the deterioration mechanisms, and the results are tabulated in Tables 6 and 7. Three-dimensional topographies and two-dimensional profiles of the wear traces on the Ti6Al4V alloy and TO layer surfaces were obtained by using a white-light interferometer, as given in Fig. 21, 22, 24 and 25.

As presented in Fig. 20(a), the wear trace of the Ti6Al4V alloy is continuous and complete. The higher magnified images in Fig. 20(c) and (e) highlight the significant corrosive-wear that occurred during sliding. There is evidence of plastic deformation on the corrosive-worn surface of the Ti6Al4V alloy, and the worn surface was very rough, characterized by adhesive craters, tearing and grooves/scratches, as revealed in Fig. 20(c) and (e). When the Ti6Al4V alloy was sliding with itself or other metallic

materials, plastic deformation and adhesion junctions frequently appeared between the contacts due to the low surface hardness of the Ti6Al4V alloy and the high chemical affinity between the "metal–metal" friction interface. However, this kind of link with insufficient bonding strength might be torn by a relative sliding of the friction pairs and result in adhesive wear.[96] In addition, the GCr15 steel was harder than the Ti6Al4V alloy, and asperities on GCr15 exerted a significant ploughing effect on the Ti6Al4V alloy. The formed grooves/scratches were wide, deep and distinguished from the grinding scratches shown in Fig. 4, which means that the Ti6Al4V alloy also suffered abrasive wear in the course of sliding wear.[97,98] The main wear manner of the Ti6Al4V alloy under this condition can be set as the adhesive wear and abrasive wear.

Fig. 20(b) displays the whole feature of the wear trace TO layer, and it is seen that the wear trace of the TO layer was narrower than that of the Ti6Al4V alloy in Fig. 20(a). As shown in Fig. 20(d) and (f), the worn surface was relatively smooth, and the damage degree was not as severe as Ti6Al4V in Fig. 20(c) and (e). Some "dark plaques" can be found in the wear trace. According to the EDS analysis of the corrosive worn TO layer surface in Table 6, it is certain that the TO layer was not worn through. The dark plaque (zone 2) corresponded to Fe-rich area, whereas the other regions

mainly contained O and Ti, indicating material transfer from the GCr15 counterpart to the TO layer. Combining the mass loss results, the wear mode of the TO layer was mainly the adhesive transfer of counter body material, and this might be attributed to the lower hardness of GCr15 in comparison with the TO layer.

As demonstrated in Fig. 21 and 22, it is clearly seen that a shallower and narrower wear trace was formed on the TO layer than that of the Ti6Al4V alloy. The transfer behaviour of GCr15 onto the TO layer was also further confirmed by Fig. 21 and 22.

As shown in Fig. 23(a) and (b), it is clear that the width of the Ti6Al4V alloy was far higher than that of the TO layer when the sliding tests were conducted against Si_3N_4. Seen from the higher magnification images of the wear traces (Fig. 23(c–f)), there were remarkable differences between the wear traces of the Ti6Al4V alloy and TO layer. As presented in Fig. 23(c) and (e), numerous parallel deep grooves and spalled holes were observed on the wear trace of the Ti6Al4V alloy. Asperities on Si_3N_4 had a ploughing effect on the soft Ti6Al4V alloy surface and left ploughing grooves on the worn surface. Meanwhile a "ceramic-
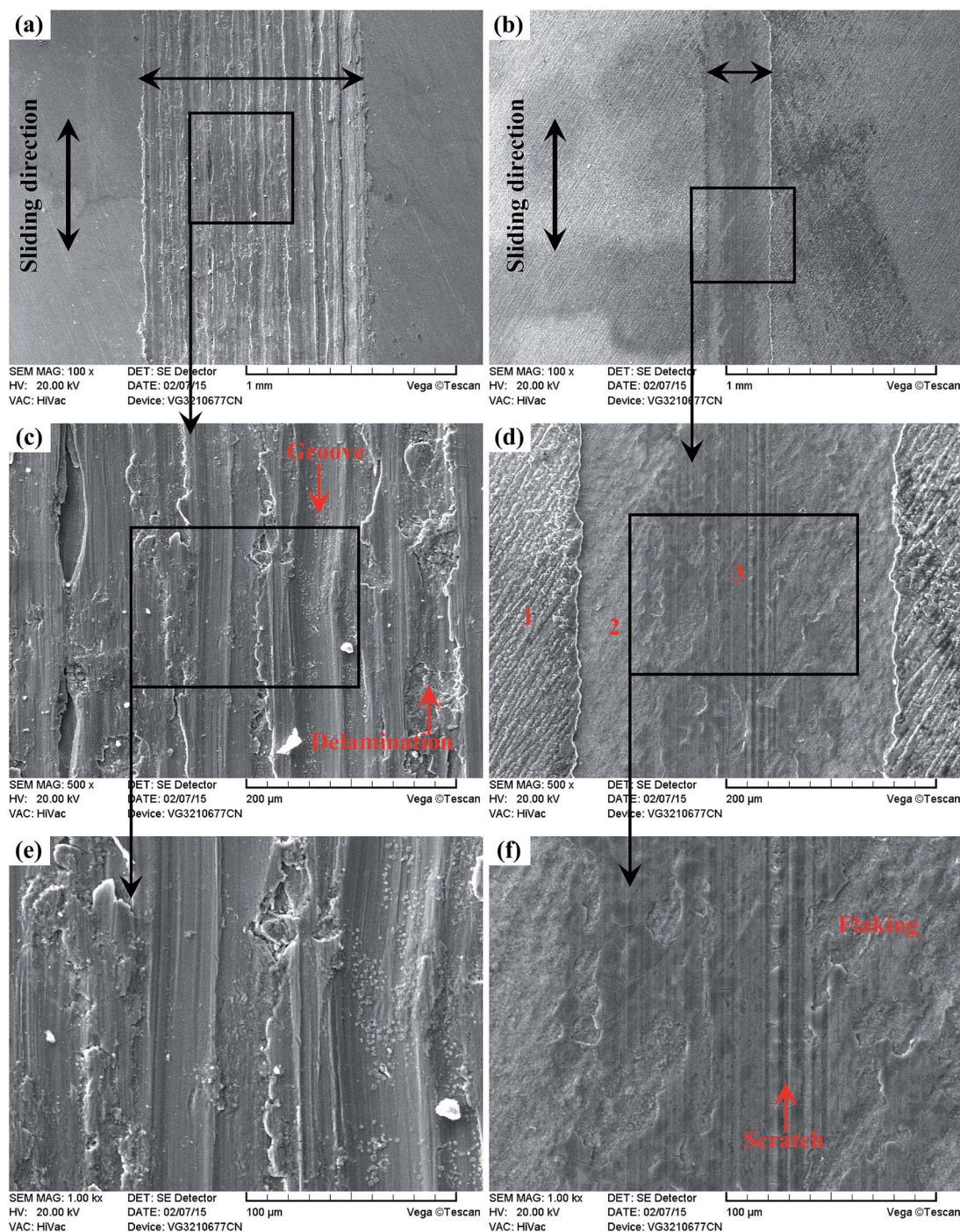

Fig. 23 Wear traces of the Ti6Al4V alloy (a) (c) (e) and TO layer (b) (d) (f) sliding against Si_3N_4.

metal" contact interface was less likely to induce adhesive wear. As the Si_3N_4 ball was much harder than the Ti6Al4V alloy, plastic deformation took place on the Ti6Al4V alloy under the actions of load and friction force. There was a dislocation pileup region on the near surface, which worked to induce the initiation of micro-cracks underneath the surface.[96–98] The cracks gradually propagated with the development of plastic deformation as the cracks extended to the surface. As a result, thin and long wear sheets were formed and spalled from the surface. The wear sheets were ground into small size abrasive particles by the relative motion of friction pairs, and abrasive wear occurred.[96–98] Thereby, the wear mechanism of the Ti6Al4V alloy was a composite form of delamination and abrasive wear.

Seen from Fig. 23(d) and (f), the worn surface of the TO layer was smoother than that of the Ti6Al4V alloy, and shallow scratches and local flaking were found in the wear trace. The TO layer had a higher hardness value than that of the Ti6Al4V alloy, and the TO layer was subjected to cyclic loading during the sliding. The cyclic loading had an effect on the initiation and growth of the fatigue crack. Once the crack propagation ran to a degree, flaking off appeared on the worn surface.[57,96–98] Si_3N_4 possesses a higher hardness and higher chemical stability, and

the TO layer was going to be worn. Compared with the Ti6Al4V alloy, a higher hardness on the surface of the TO layer could reduce the wearing damage from Si_3N_4, but asperities on Si_3N_4 still played a ploughing effect on the TO layer surface and left scratches. The main wear mechanism of the TO layer was fatigue wear and slight abrasive wear (scratching). Based on the EDS analysis of the typical zones on the corrosive worn TO layer surface in Table 7, it is certain that the TO layer was not totally worn through after sliding against Si_3N_4. Seen from Fig. 24 and 25, it is obvious that the Ti6Al4V alloy suffered more serious damage than the TO layer, and a much shallower and narrower wear trace was found on the TO layer surface than that of the Ti6Al4V alloy.

Since the wear trace profiles were suggested in Fig. 22 and 25, the specific wear rate of each tested sample can be calculated through the following equation:[99]

$$K = \frac{V_w}{FD} \tag{6}$$

Where K is the specific wear rate ($mm^3\ N^{-1}\ m^{-1}$), V_w is the wear volume (mm^3), F is the given load (N) and D is the sliding distance (m).
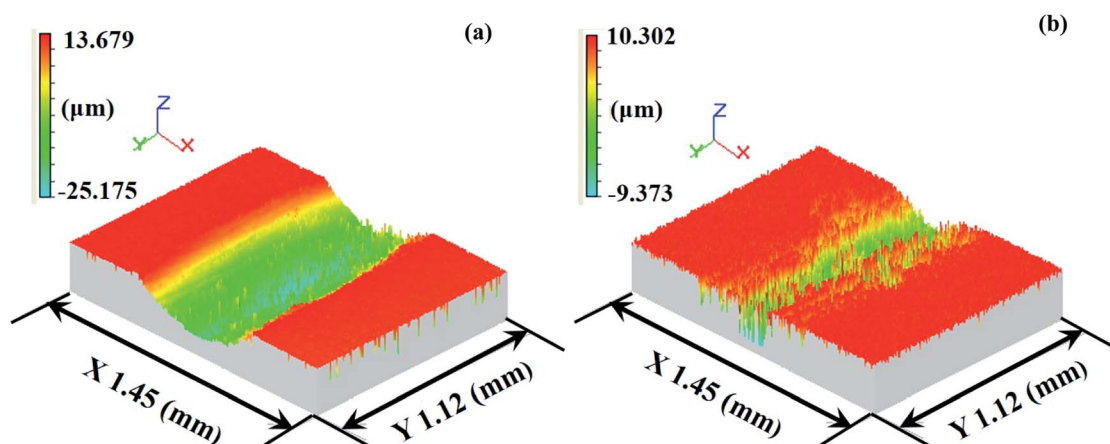

Fig. 24 White-light interferometer wear traces of the Ti6Al4V alloy (a) and TO layer (b) sliding against Si_3N_4.
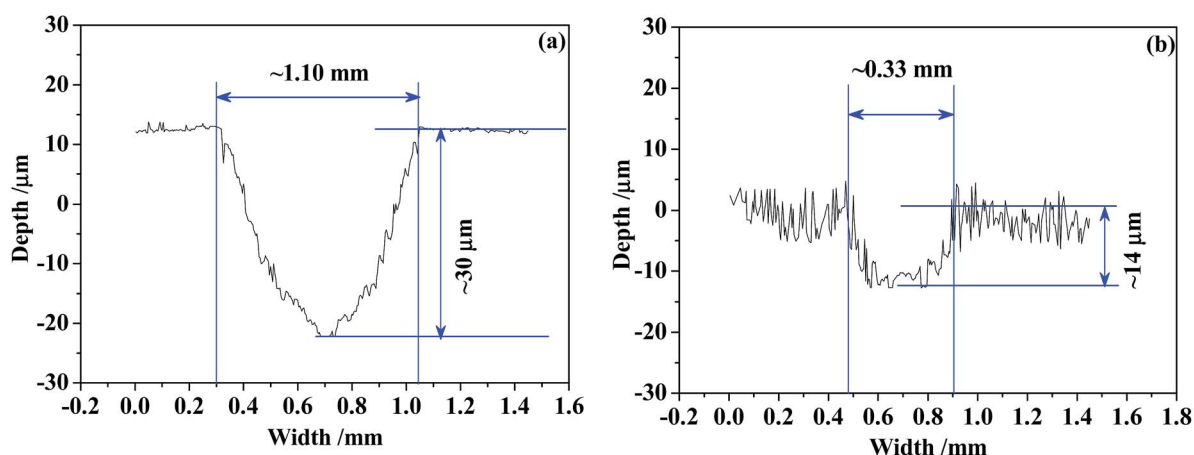

Fig. 25 Wear trace profiles of the Ti6Al4V alloy (a) and TO layer (b) sliding against Si_3N_4.

Table 8 Results of friction and wear tests

Counterpart-sample result	GCr15		Si$_3$N$_4$	
	Ti6Al4V	TO layer	Ti6Al4V	TO layer
COF (μ)	0.35	0.40	0.25	0.20
Mass loss/mg	0.38	-0.10	0.33	0.19
h/μm	$\sim$21	$\sim$11	$\sim$30	$\sim$14
b/mm	$\sim$1.00	$\sim$0.67	$\sim$1.10	$\sim$0.33
V_w/mm^3	$\sim$0.0700	$\sim$0.0246	$\sim$0.110	$\sim$0.0154
K/mm^3 N^{-1} m^{-1}	$\sim$1.94 $\times$ 10^{-4}	$\sim$6.83 $\times$ 10^{-5}	$\sim$3.16 $\times$ 10^{-4}	$\sim$4.28 $\times$ 10^{-5}

The V_w in eqn (6) can be obtained by eqn (7) as follows:[100]

$$V_w = \frac{ah(3h^2 + 4b^2)}{6b} \tag{7}$$

Where a is the length of the wear trace (mm), h is the depth of the wear trace (μm) and b is the width of the wear trace (mm). By plugging in the known quantities of a, h and b into eqn (7), one can calculate the results of the values of K, as indicated together with the COF and mass losses in Table 8. It was certain that the TO layer held better corrosive-wear resistance than the Ti6Al4V alloy. Meanwhile as indicated above in the cross-sectional morphology (Fig. 7) and GDOES composition profile–distance from the surface (Fig. 8), the thickness of the TO layer was deeper than the depth of its wear trace (see Fig. 24 and 25), and the TO layer provided a considerable protective effect on the Ti6Al4V alloy from another point of view.

4. Conclusions

A TO layer was fabricated onto a Ti6Al4V alloy at 700 °C for 30 h to improve the surface performance and prolong its service lifetime. A continuous and compact TO layer with a total thickness of about 20 μm was produced. The TO layer was mainly composed of rutile phase TiO$_2$ and minor anatase phase TiO$_2$. There was also an obviously external migration process of Al during the TO process. The concentration of O presented a gradient distribution along the thickness of the TO layer. TO treatment improved the surface hardness of the Ti6Al4V alloy, and the TO layer was well bonded with the substrate. By comparing E_{corr}, I_{corr} and I_{pass} data, it was found that the TO layer had better corrosion resistance than the raw Ti6Al4V alloy. The TO layer could provide considerable protective effects on the Ti6Al4V alloy in erosive-wear and corrosive-wear tests. The excellent erosive-wear and corrosive-wear performance of the TO layer benefited from its good chemical stability, mechanical isolation action, high hardness and promising bonding strength. TO treated Ti6Al4V alloy has great potential to be used as petroleum tubes for oil and gas exploitation applications.

Acknowledgements

Notes and references

1 M. A. Vasylyev, S. P. Chenakin and L. F. Yatsenko, *Acta Mater.*, 2012, **60**, 6223–6233.
2 L. L. Liu, J. Xu, P. Munroe and Z. H. Xie, Microstructure, *Electrochim. Acta*, 2014, **115**, 86–95.
3 S. M. Yu, D. X. Liu, X. H. Zhang and D. X. Du, *Appl. Surf. Sci.*, 2015, **353**, 995–1002.
4 F. C. Liu, Y. Q. Mao, X. Lin, B. S. Zhou and T. Qian, *Opt. Laser Technol.*, 2016, **83**, 140–147.
5 X. H. Lu, Y. Shu, G. Zhao, J. Xie and Y. Xue, *Rare Met. Mater. Eng.*, 2014, **43**, 1518–1524.
6 R. W. Schutz and H. B. Watkins, *Mater. Sci. Eng., A*, 1998, **243**, 305–315.
7 D. G. Bansal, O. L. Eryilmaz and P. J. Blau, *Wear*, 2011, **271**, 2006–2015.
8 L. L. Guo, L. Qin, F. Y. Kong, H. Yi and B. Tang, *Appl. Surf. Sci.*, 2016, **388**, 203–211.
9 Y. S. Tian, C. Z. Chen, S. T. Li and Q. H. Huo, *Appl. Surf. Sci.*, 2005, **242**, 177–184.
10 N. M. Lin, H. Y. Zhang, J. J. Zou and B. Tang, *Rev. Adv. Mater. Sci.*, 2014, **38**, 61–74.
11 İ. Çelik and M. Karakan, *Kovove Mater.*, 2016, **54**, 37–43.
12 X. Y. Liu, P. K. Chu and C. X. Ding, *Mater. Sci. Eng., R*, 2004, **47**, 49–121.
13 Z. X. Wang, H. R. Wu, X. L. Shan, N. M. Lin, Z. Y. He and X. P. Liu, *Appl. Surf. Sci.*, 2016, **388**, 510–516.
14 M. S. Mahdipoor, D. Kevorkov, P. Jedrzejowski and M. Medraj, *Surf. Coat. Technol.*, 2016, **292**, 78–89.
15 İ. Çelik, M. Karakan and F. BüIbüI, *Proc. Inst. Mech. Eng., Part J*, 2016, **230**, 57–63.
16 T. Balusamy, T. S. N. Sankara Narayanan, K. Ravichandran, I. S. Park and M. H. Lee, *Corros. Sci.*, 2013, **230**, 332–344.
17 *Surface Coatings for Protection against Wear*, ed. B.G. Mellor, Woodhead Publishing Limited, Cambridge, England, 2006.
18 F. Muhaffel, G. Cempura, M. Menekse, A. Czyrska-Filemonowicz, N. Karaguler and H. Cimenoglu, *Surf. Coat. Technol.*, 2016, **307**, 308–315.
19 S. Durdu and M. Usta, *Ceram. Int.*, 2014, **40**, 3627–3635.

20 P. Trivedi, P. Gupta, S. Srivastava, R. Jayaganthan, R. Chandra and P. Roy, *Appl. Surf. Sci.*, 2014, **293**, 143–150.

21 L. Joska, J. Fojt, O. Mestek, L. Cvrcek and V. Brezina, *Surf. Coat. Technol.*, 2012, **206**, 4899–4906.

22 T. R. Rautray, R. Narayanan and K. H. Kim, *Prog. Mater. Sci.*, 2011, **56**, 1137–1177.

23 E. Marcelli, M. L. Costantino, T. Villa, P. Bagnoli, R. Zannoli, I. Corazza and L. Cercenelli, *J. Prosthet. Dent.*, 2014, **112**, 1201–1211.

24 W. Yan and X. X. Wang, *J. Mater. Sci.*, 2004, **39**, 5583–5585.

25 M. Das, V. K. Balla, D. Basu, I. Manna, T. S. S. Kumar and A. Bandyopadhyay, *Scr. Mater.*, 2012, **66**, 578–581.

26 C. B. Tang, D. X. Liu, Z. Wang and Y. Gao, *Appl. Surf. Sci.*, 2011, **257**, 6364–6371.

27 J. G. Tang, D. X. Liu, X. H. Zhang, D. X. Du and S. M. Yu, *Materials*, 2016, **9**, 217–221.

28 K. Chen, X. P. Liu, X. Z. Liu, T. X. Meng, Q. Guo, Z. X. Wang and N. M. Lin, *J. Wuhan Univ. Technol., Mater. Sci. Ed.*, 2016, **31**, 1086–1092.

29 Ç. Albayrak, İ. Hacısalihoğlu, S. Y. Vangölü and A. Alsaran, *Wear*, 2013, **302**, 1642–1648.

30 M. R. Ripoll, R. Simič, J. Brenner and B. Podgornik, *Tribol. Lett.*, 2013, **51**, 261–271.

31 A. Biswas and J. D. Majumdar, *Mater. Charact.*, 2009, **60**, 513–518.

32 A. Ashrafizadeh and F. Ashrafizadeh, *J. Alloys Compd.*, 2009, **480**, 849–852.

33 S. Frangini, A. Mignone and F. De Riccardis, *J. Mater. Sci.*, 1994, **29**, 714–720.

34 E. Arslan, Y. Totik, E. Demirci and A. Alsaran, *J. Mater. Eng. Perform.*, 2010, **19**, 428–433.

35 Y. Luo, W. W. Chen, M. C. Tian and S. S. Teng, *Tribol. Int.*, 2015, **89**, 67–71.

36 S. Wang, Z. H. Liao, Y. H. Liu and W. Q. Liu, *Mater. Chem. Phys.*, 2015, **159**, 139–151.

37 M. C. García-Alonsoa, L. Saldaña, G. Vallés, J. L. González-Carrasco, J. González-Cabrero, M. E. Martínez, E. Gil-Garay and L. Munuera, *Biomaterials*, 2003, **24**, 19–26.

38 N. Somsanith, T. S. N. Sankara Narayanan, Y. K. Kim, I. S. Park, T. S. Bae and M. H. Lee, *Appl. Surf. Sci.*, 2015, **356**, 1117–1126.

39 H. Dong and T. Bell, *Wear*, 2000, **238**, 131–137.

40 H. Guleryuz and H. Cimenoglu, *J. Alloys Compd.*, 2009, **472**, 241–246.

41 F. Billi, E. Onofre, E. Ebramzadeh, T. Palacios, M. L. Escudero and M. C. Garcia-Alonso, *Surf. Coat. Technol.*, 2012, **212**, 134–144.

42 H. Guleryuz and H. Cimenoglu, *Surf. Coat. Technol.*, 2005, **192**, 164–170.

43 S. Wang, Z. H. Liao, Y. H. Liu and W. Q. Liu, *Surf. Coat. Technol.*, 2014, **240**, 470–477.

44 F. Borgioli, E. Galvanetto, F. Iozzelli and G. Pradelli, *Mater. Lett.*, 2005, **59**, 2159–2162.

45 A. Ravi Shankar, N. S. Karthiselva and U. Kamachi Mudali, *Surf. Coat. Technol.*, 2013, **235**, 45–53.

46 M. Jamesh, S. Kumar, T. S. N. Sankara Narayanan and P. K. Chu, *Mater. Corros.*, 2013, **64**, 902–907.

47 S. Kumar, T. S. N. Sankara Narayanan, S. Ganesh Sundara Raman and S. K. Seshadri, *Mater. Chem. Phys.*, 2010, **119**, 337–346.

48 H. Cimenoglu, O. Meydanoglu, M. Baydogan, H. Bermek, P. Huner and E. S. Kayali, *Met. Mater. Int.*, 2011, **17**, 765–770.

49 P. A. Dearnley, K. L. Dahm and H. Çimenoğlu, *Wear*, 2004, **256**, 469–479.

50 H. Güleryüz and H. Çimenoğlu, *Biomaterials*, 2004, **25**, 3325–3333.

51 A. R. Ebrahimi, F. Zarei and R. A. Khosroshahi, *Surf. Coat. Technol.*, 2008, **203**, 199–203.

52 Z. X. Zhang, H. S. Dong, T. Bell and B. S. Xu, *J. Alloys Compd.*, 2007, **431**, 93–99.

53 Q. C. Sun, T. C. Hu, H. Z. Fan, Y. S. Zhang and L. T. Hu, *Tribol. Int.*, 2016, **94**, 479–489.

54 M. A. Vasylyev, S. P. Chenakin and L. F. Yatsenko, *Acta Mater.*, 2016, **103**, 761–774.

55 C. S. Brandolt, M. R. Ortega Vega, T. L. Menezes, R. M. Schroeder and C. F. Malfatti, *Mater. Corros.*, 2016, **67**, 368–377.

56 J. J. Zou, N. M. Lin, L. Qin, B. Tang and F. Q. Xie, *Surf. Rev. Lett.*, 2013, **20**, 1330002–1330011.

57 N. M. Lin, F. Q. Xie, H. J. Yang, W. Tian, H. F. Wang and B. Tang, *Appl. Surf. Sci.*, 2012, **258**, 4960–4970.

58 L. N. Xu, B. Wang, J. Y. Zhu, W. Li and Z. Y. Zheng, *Appl. Surf. Sci.*, 2016, **379**, 39–46.

59 C. Q. Ren, D. X. Liu, Z. Q. Bai and T. H. Li, *Mater. Chem. Phys.*, 2005, **93**, 305–309.

60 W. L. Rong, H. J. Hei, Q. Zhong, Y. Y. Shen, X. P. Liu, X. Wang, B. Zhou, Z. Y. He and S. W. Yu, *Appl. Surf. Sci.*, 2015, **359**, 41–47.

61 J. Xu and C. Zhuo, *Mater. Corros.*, 2010, **61**, 368–377.

62 J. Xu, C. Z. Zhuo, D. Z. Han, J. Tao, L. L. Liu and S. Y. Jiang, *Corros. Sci.*, 2009, **51**, 1055–1068.

63 K. Yang, J. Rong, C. G. Liu, H. Y. Zhao, S. Y. Tao and C. X. Ding, *Tribol. Int.*, 2016, **93**, 29–35.

64 C. S. Ramesh, N. Sekhar, R. Keshavamurthy and S. Pramod, *Int. J. Surf. Sci. Eng.*, 2015, **9**, 55–68.

65 R. C. Shivamurthy, M. Kamaraj, R. Nagarajan, S. M. Shariff and G. Padmanabham, *Wear*, 2009, **267**, 204–212.

66 C. I. Walker and M. Hambe, *Wear*, 2015, **332–333**, 1021–1027.

67 N. M. Lin, F. Q. Xie, J. J. Zou and B. Tang, *Sci. China: Technol. Sci.*, 2013, **56**, 1415–1423.

68 M. Ramachandrai and K. Radhakrishna, *Mater. Sci.-Pol.*, 2006, **24**, 333–349.

69 M. Nouri, X. G. Sun and D. Y. Li, *Tribol. Int.*, 2013, **67**, 154–163.

70 A. H. Yaghtin, E. Salahinejad, A. Khosravifard, A. Araghi and A. Akhbarizadeh, *Ceram. Int.*, 2015, **41**, 7916–7920.

71 C. X. Ouyang, S. G. Zhu and D. Y. Li, *J. Alloys Compd.*, 2014, **615**, 146–155.

72 N. M. Lin, P. Zhou, Y. T. Wang, J. J. Zou, Y. Ma, Z. Wang, W. Tian, X. F. Yao and B. Tang, *Surf. Rev. Lett.*, 2015, **22**, 1550033–1550041.

73 H. Güleryüz, E. Atar, F. Seahjani and H. Çimenoğlu, *Diffus. Found.*, 2015, **4**, 103–116.

74 M. S. El-Eskandrany and A. Al-Azmi, *J. Mech. Behav. Biomed. Mater.*, 2016, **56**, 183–194.

75 S. Wang, Z. H. Liao and Y. H. Liu, *Chin. J. Nonferrous Met.*, 2014, **24**, 1466–1473.

76 J. Z. Tang, Q. Ding, S. W. Zhang, G. Z. Wu and L. T. Hu, *Materials*, 2016, **9**, 795–801.

77 A. M. Oladoye, J. G. Carton, K. Benyounis, J. Stokes and A. G. Olabi, *Surf. Coat. Technol.*, 2016, **304**, 384–392.

78 S. Wang, Y. H. Liu, C. X. Zhang, Z. H. Liao and W. Q. Liu, *Tribol. Int.*, 2014, **79**, 174–182.

79 J. J. Si, X. H. Chen, Y. H. Cai, Y. D. Wu, T. Wang and X. H. Hui, *Corros. Sci.*, 2016, **107**, 123–132.

80 D. J. Young, *High Temperature Oxidation and Corrosion of Metals*, Elsevier, Amsterdam, Netherlands, 2016.

81 M. M. Zhang, M. L. Shen, L. Xin, X. Y. Ding, S. L. Zhu and F. H. Wang, *Corros. Sci.*, 2016, **112**, 36–43.

82 V. Mannava, A. S. Rao, N. Paulose, M. Kamaraj and R. S. Kottada, *Corros. Sci.*, 2016, **105**, 109–119.

83 M. A. Lodes, S. Sailer, S. M. Rosiwal and R. F. Singer, *Appl. Surf. Sci.*, 2013, **282**, 335–341.

84 T. Wang, H. Zhuang and X. Jiang, *Appl. Surf. Sci.*, 2015, **359**, 790–796.

85 M. Jamesh, S. Kumar and T. S. N. Sankara Narayanan, *J. Mater. Eng. Perform.*, 2012, **21**, 900–906.

86 N. M. Lin, M. L. Li, J. J. Zou, X. G. Wang and B. Tang, *J. Mater. Eng. Perform.*, 2013, **22**, 1365–1370.

87 N. W. Dai, L. C. Zhang, J. X. Zhang, X. Zhang, Q. Z. Ni, Y. Chen, M. L. Wu and C. Yang, *Corros. Sci.*, 2016, **111**, 703–710.

88 Z. B. Zheng and Y. G. Zheng, *Corros. Sci.*, 2016, **112**, 657–668.

89 J. Xu, H. J. Huang, Z. Y. Li, S. Xu, H. L. Tao, P. Munroe and Z. H. Xie, *J. Alloys Compd.*, 2016, **663**, 718–730.

90 S. Dehgahi, R. Amini and M. Alizadeh, *J. Alloys Compd.*, 2017, **692**, 622–628.

91 V. Niksefat and M. Ghorbani, *J. Alloys Compd.*, 2015, **633**, 127–136.

92 M. Zhao, J. D. Wang, D. R. Chen, X. P. Hao and B. Y. Wang, *J. Alloys Compd.*, 2008, **466**, 421–428.

93 X. L. Ji, J. H. Zhao, X. W. Zhang and M. Y. Zhou, *Tribol. Int.*, 2013, **60**, 19–24.

94 K. Aniołek, M. Kupka, A. Barylski and G. Dercz, *Appl. Surf. Sci.*, 2015, **357**, 1419–1426.

95 J. Qu, P. J. Blau, T. R. Watkins, O. B. Cavin and N. S. Kulkarni, *Wear*, 2005, **258**, 1348–1356.

96 N. M. Lin, Q. Liu, J. J. Zou, J. W. Guo, D. L. Li, S. Yuan, Y. Ma, Z. X. Wang, Z. H. Wang and B. Tang, *Materials*, 2016, **9**, 875–881.

97 B. A. Obadele, A. Andrews, M. B. Shongwe and P. A. Olubambi, *Mater. Chem. Phys.*, 2016, **171**, 239–246.

98 Y. Zhang, X. Y. Yin and F. Y. Yan, *Mater. Chem. Phys.*, 2016, **179**, 273–281.

99 P. C. Yu, X. B. Liu, X. L. Lu, S. J. Qiao, Y. J. Zhai, G. X. Zhu, Y. G. Wang and Y. Chen, *RSC Adv.*, 2015, **5**, 76516–76525.

100 Y. L. Zhang, X. Y. Luo and F. He, *Rare Met. Mater. Eng.*, 2013, **42**, 204–210.